

Gold Deposition at a Free-Standing Liquid/Liquid Interface: Evidence for the Formation of Au(I) by Microfocus X-ray Spectroscopy (μ XRF and μ XAFS) and Cyclic Voltammetry

Samuel G. Booth,[†] Akihiro Uehara,[‡] Sin Yuen Chang,[§] J. Fred W. Mosselms,^{||} Sven L. M. Schroeder,^{*,[⊥]} and Robert A. W. Dryfe^{*,[†]}

[†]School of Chemistry, The University of Manchester, Oxford Road, Manchester M13 9PL, U.K.

[‡]Division of Nuclear Engineering Science, Research Reactor Institute, Kyoto University, Asashironishi, Kumatori, Osaka 590-0494, Japan

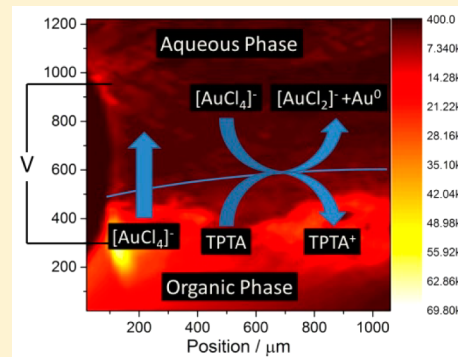
[§]School of Chemical Engineering and Analytical Science, The University of Manchester, Oxford Road, Manchester M13 9PL, U.K.

^{||}Diamond Light Source Ltd., Didcot, Oxfordshire OX11 0DE, U.K.

[⊥]School of Chemical and Process Engineering, University of Leeds, Leeds LS2 9JT, U.K.

S Supporting Information

ABSTRACT: Electrochemical gold nucleation and nanoparticle growth at a liquid/liquid interface were examined in situ by combined X-ray fluorescence (XRF) mapping with a microfocus X-ray beam and X-ray absorption fine structure (XAFS) spectroscopy. Gold deposition was achieved by reduction of $[\text{AuCl}_4]^-$ with tri-*p*-tolylamine at a water/1,2-dichlorobenzene interface using a windowless liquid/liquid interface system formed from the contact of aqueous and organic phase droplets. The combination of XRF and XAFS, with a spatial resolution of approximately $70 \mu\text{m}$, provided chemical speciation information near the interface under gold deposition conditions. Analysis of the X-ray absorption near-edge structure (XANES) reveals evidence for the presence of Au(I) species as a reduction intermediate, concomitant with a buildup of metallic gold at the interface. Cyclic voltammetry indicates the presence of two ion transfer peaks at the liquid/liquid interface, which are assigned to the transfer of $[\text{AuCl}_4]^-$ and $[\text{AuCl}_2]^-$. Finally ex situ TEM analysis shows that the resultant nanoparticles have an average size between 3 and 4 nm. In line with this particle size, the XAFS indicates bulk-like structure.



1. INTRODUCTION

A number of efficient, solution-phase strategies for the preparation of metallic nanoparticles, generally by reduction of the corresponding metal ion, now exist.^{1–6} Gold nanoparticles are among the most widely studied of this class of materials. Current interest has shifted to understanding the mechanism of these particle growth processes, both to enable further optimization of particle preparation and because of the associated scientific insights.^{7–10} Nanoparticle formation by spontaneous (i.e., chemical) reduction is possible in single and two-phase systems.^{1–4} Similarly, electrochemical control over deposition is possible on solid surfaces^{11–14} or in a two-phase liquid/liquid (water/immiscible organic solvent) system forming particles at the interface.¹⁵ The liquid/liquid interface offers a defect-free, repairable point for nucleation and growth which may provide new information about the deposition process. Various metals have been generated in nanoparticulate form by growth at the interface between two immiscible electrolyte solutions (ITIES), including Pt, Pd, Cu, Ag, Au, and core-shell particles (Au@Cu).^{15–21} In this case particles can be formed either under external potential control, i.e., using a four-

electrode potentiostatic setup, or by interfacial potential control through use of a “common ion”, where the ionic partition equilibrium determines the potential.

For gold reduction, there has been a substantial discussion about the mechanism of the process, specifically on whether it follows a two-electron reduction from Au(III) to Au(I) or whether a direct three-electron reduction to Au metal occurs and to what extent the reduction process is influenced by disproportionation of Au(I) to Au(III) and Au(0) or of the reverse comproportionation.²² On thermodynamic grounds, Au(I) should form at room temperature via comproportionation as a minor component in aqueous solutions with low ($<10^{-3}$ M) gold concentrations or high (>1 M) chloride concentrations;²² otherwise, in aqueous solution at room temperature, the reverse disproportionation of $[\text{AuCl}_2]^-$ dominates.²³ The kinetic stability of Au(I) has also been a subject of discussion: our most recent electrochemical and XAS

Received: May 29, 2015

Revised: July 1, 2015

Published: July 1, 2015

work suggests that $[\text{AuCl}_2]^-$ is stable in organic solvent.^{24,25} This insight is consistent with the demonstration that Au(I) species are an intermediate in the “Brust–Schiffrin” thiol-mediated reduction of Au(III) to nanoparticulate Au,^{8–10} a two-phase process where the initial Au reduction is performed in the organic (normally toluene) phase.^{3,4} Although Au(I) is not usually considered as an intermediate in the electrochemical reduction of Au(III) in aqueous solution, *vide infra*, it has been proposed as an intermediate species in some aqueous reduction processes, for example in the pulse radiolytic reduction of $[\text{AuCl}_4]^-$.²⁶ A further complexity with regard to the speciation of Au(I) and Au(III) in aqueous solutions is the pH-dependent stability of the halide ligands. In aqueous solutions above pH 5, $[\text{AuCl}_4]^-$ undergoes partial hydrolysis, with $[\text{AuCl}_3(\text{OH})]^-$ becoming the predominant species in solution.²⁷ Similar hydrolysis processes exist for $[\text{AuCl}_2]^-$ at acidic pHs and/or low chloride concentrations.²³

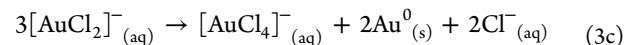
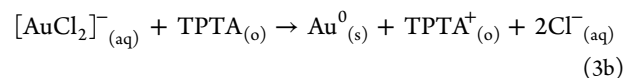
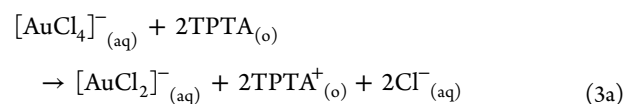
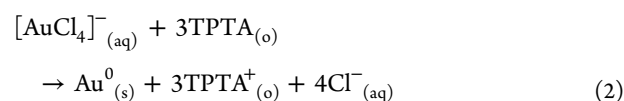
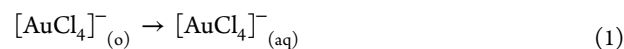
With regard to the electrochemical reduction of Au(III), cyclic voltammetry (CV) has generally been used as a tool for mechanistic studies, although peak assignment for the deposition process can be complicated when multiple processes occur in the system. In aqueous solutions the three-electron reduction from Au(III) to Au(0) has been proposed for the case of boron-doped diamond electrodes in acidic solution.²⁸ Similarly, the direct three-electron mechanism was concluded to be the dominant process for Au deposition from concentrated chloride solutions on carbon (glassy carbon and pyrolytic graphite) surfaces.²² Other studies of Au deposition on graphite from concentrated aqueous chloride²⁹ and perchlorate solutions,³⁰ respectively, have noted that the process was “complex” but avoided discussion of the operative deposition mechanism by writing the deposition process as a “global” three-electron discharge. As with the case of chemical reduction of Au(III), there appears to be a contrast in the operative electroreduction mechanisms for Au(III) in non-aqueous solutions, with the consensus that the Au(I) intermediate is involved. For example, deposition of $[\text{AuCl}_4]^-$ onto a Au electrode from acetonitrile solution was reported to proceed via $[\text{AuCl}_2]^-$, and similarly the oxidation of the Au electrode in the presence of chloride electrolyte reportedly formed $[\text{AuCl}_2]^-$.³¹ Comparable behavior has been reported for Au(I) species in chloride electrolytes in dichloromethane³² and for electrodeposition of $[\text{AuCl}_4]^-$ from an imidazolium-based ionic liquid, which again is reported to proceed via an $[\text{AuCl}_2]^-$ intermediate.³³ The above works on the nonaqueous electrochemistry of Au(I) rely solely on electrochemical data for the assignment of reaction mechanisms. An exception to this approach is work on Au deposition from $[\text{AuCl}_4]^-$ using dimethyl sulfoxide and an ammonium-based ionic liquid as solvent,³⁴ where some microscopic characterization of the deposited Au was performed. As has been noted previously,^{34–36} a significant factor underlying the differences in Au halide stability seen in aqueous, compared to nonaqueous, media is the solvation energy of the halide liberated on Au reduction. Specifically, the more favorable solvation energy of halides in water means that the reduction potential of the Au(III)/Au(0) couple is depressed on transfer to nonaqueous media. This solvent dependence of reduction potential becomes important if deposition is performed under electrochemical control at the liquid/liquid interface, where the precursor ion can distribute among both phases. This approach to metal deposition was first applied to Au using organic phase $[\text{AuCl}_4]^-$ reduced by aqueous phase ferrocyanide.¹⁵

In the present manuscript, we examine the deposition of Au at the liquid/liquid interface by using a relatively stable electron donor, tri-*p*-tolylamine (TPTA) which does not reduce $[\text{AuCl}_4]^-$ when the ion is present in the organic phase, whereas reduction can occur spontaneously when the ion is transferred to the aqueous phase, due to the reduction potentials’ sensitivity to solvent.³⁶ Application of a potential pulse to drive ion transfer thus led to the interfacial nucleation of Au nanoparticles using TPTA as an organic phase electron donor. Cyclic voltammetry was carried out to examine the transfer of the ionic reactants and intermediates across the liquid/liquid interface. The electrochemical data are combined with X-ray absorption spectroscopy (XAS), due to the sensitivity of this technique to metal oxidation states in solution.

Microfocus X-ray beams permit studies of Au speciation with high spatial resolution.³⁷ We have recently demonstrated the viability of this approach in a study of the metal deposition process at a liquid/liquid interface, combining microfocus X-ray fluorescence (μXRF) and microfocus X-ray absorption fine structure (μXAFS) with UV–vis spectroscopy in the home laboratory.³⁸ In the present work we use the same approach to examine the interfacial nanoparticle formation process in order to determine the reduction sequence and also to examine the spatial variation seen in this system, with the specific aim of identifying the role of Au(I).

2. RESULTS

2.1. Microfocus X-ray Fluorescence (μXRF) Mapping of the Liquid/Liquid Interface. The possible reactions for the reduction of $[\text{AuCl}_4]^-$ by TPTA are shown in eqs 1–3. In the equations (aq) is the aqueous phase, (o) the organic, and (s) a solid.³⁸



The reaction may either proceed via a direct reduction from Au(III) to Au(0) (eqs 1 and 2) or via a Au(I) intermediate (eqs 1 and 3). TPTA has been shown to form a very stable cation; therefore, a single electron transfer is assumed for each molecule.³⁹ It is this likelihood of stepwise one-electron reductions that raises the possibility that Au(I) species may be formed alongside Au(0). Au(I) may then be reduced to Au(0) by TPTA or undergo disproportionation (eq 3c). As noted in the Introduction, the deposition process is driven by the transfer of the Au(III) species into the aqueous phase, due to the higher reduction potential of the tetrachloroaurate species on transfer to water.³⁶

μXRF maps of the liquid/liquid interface and the adjacent solution phases were acquired to determine the distribution of

Au. Figure 1 shows a map acquired after the interfacial formation of Au nanoparticles was initiated by application of a

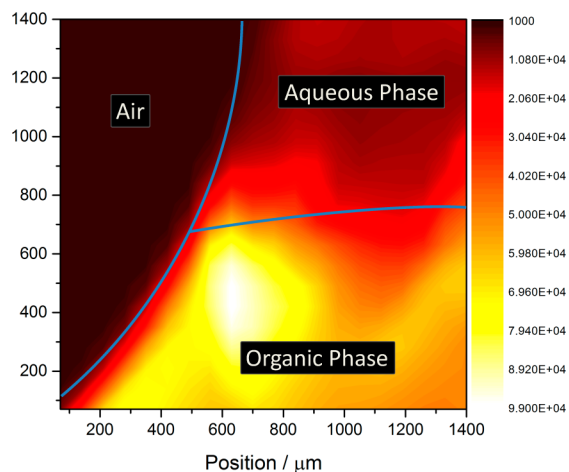


Figure 1. XRF map of the droplet cell liquid/liquid interface showing the contact made between the aqueous and organic droplets at 0.3 V following the potential pulse sequence (0.1 V for 10 s, 0.45 V for 15 s). Yellow areas show the highest L_3 fluorescence, while the black indicates low fluorescence. The darkest region to the left of the image is the vapor-saturated air adjacent to the droplet. The XRF map is annotated with lines indicating the approximate position of the phase locations.

potential pulse to the interface, defined in the Experimental Section, to induce the transfer of the tetrachloroaurate ions.³⁸ The μ XRF maps were acquired by measuring the fluorescence intensity using an incident X-ray photon energy of 12600 eV for a 1 s scan with a spatial resolution of 70 μ m. The photon energy corresponds to absorption above the Au L_3 excitation threshold and should be independent of any change in white line intensity due to oxidation state variation (see below). The intensity of emission is therefore proportional to the concentration of Au in the region of each pixel.

The yellow regions indicate high concentrations of Au, while the intermediate orange and red regions indicate lower concentrations. To determine the distribution of gold oxidation states within this heterogeneous system it is necessary to perform X-ray absorption near-edge structure (XANES) analysis. The μ XRF mapping of the interface enables targeted μ XANES in order to examine the regions of greater interest. For this study the focus was on the composition at the liquid/liquid interface, as this was the location of the reduction reaction.

2.2. Au Speciation Analysis by μ XANES. In order to quantify the relative concentrations of Au species in the system the spectra were described by a fit generated from a linear combination of the reference spectra for the Au species involved. The analysis of the spectroscopic data is based on the intensity of transitions to unoccupied 5d states in the XANES at the Au L_3 -edge (excitation of Au $2p_{3/2}$ electrons), which reflects the 5d occupancy and hence the oxidation state of the metal.⁴⁰ For Au(III) species a very intense absorption band is observed, which is often referred to as a “white line”, whereas with Au(0) barely any 5d states are unoccupied, resulting in weak absorption in this region. We have recently reported a reference spectrum for the $[\text{AuCl}_2]^-$ species in chlorinated organic solvents,²⁵ which demonstrated that the XANES of $[\text{AuCl}_2]^-$ has absorption features that distinguish it from

metallic Au and Au(III) species. The presence of metallic Au is usually distinguishable due to the presence of a large Au–Au multiple scattering peak at 11 946 eV.⁴¹

The reference spectra for $[\text{AuCl}_4]^-$, $[\text{AuCl}_2]^-$, and metallic Au are shown in Figure 2. In the following presentation of

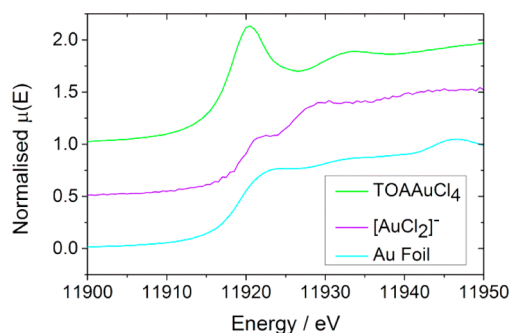


Figure 2. Au(III), Au(I), and metallic Au standards collected for linear combination analysis of the reduction process. TOAAuCl₄ was prepared as a 5 mM solution in 1,2-dichlorobenzene (DCB), and the spectrum of pure $[\text{AuCl}_2]^-$ was extracted from a 6 mM solution of tetrabutylammonium gold(I) chloride (TBAuCl₂), as detailed previously.²⁵

XANES data a linear combination fit (LCF) (red) will be provided along with the normalized experimental XANES (blue). The contributions from the reference spectra will be included as scaled components to indicate the size of their contribution to the fit, where the three contributions sum to a total of 1. The reference spectra have the following colors assigned: Au(III) (green), Au(I) (purple), Au(0) (cyan).

Full XANES scans were then taken from (i) points with very high fluorescence intensity, indicating a high Au concentration, and (ii) from positions close to the liquid/liquid interface where Au nanoparticle formation is expected to occur. Typical results are indicated in Figure 3. As anticipated from the μ XRF maps (Figure 3a and 3c), when the μ XANES is directed at a region with very high fluorescence the LCF indicates a major Au(III) contribution (83%) (Figure 3b). In the organic phase this is anticipated as a high concentration of TOAAuCl₄ was initially present. The fit also indicates the presence of fully reduced Au(0) as 17% of the gold concentration in the organic phase. The presence of a small quantity of metallic Au in the organic phase following reduction is reasonable for nanoparticles. Particle assembly at the liquid/liquid interface has been shown to reduce the overall surface energy of the system by separating the two liquid phases and forming a more stable organic/solid/aqueous interface.^{42,43} However, for nanometer-scale particles, the adsorption energy is close to $k_B T$ (Boltzmann constant and temperature, respectively), and therefore, at room temperature, some reversible particle desorption into the bulk phase would be expected.^{43,44}

The μ XANES probe was directed at the liquid/liquid interface to examine the reduction reaction, as described in the Introduction. The specific aim was to determine whether $[\text{AuCl}_2]^-$ was detectable as an intermediate during the deposition process, as seen in similar reduction reactions.²⁴ Figure 3d shows a typical spectrum obtained from the interface. LCF at this position reveals a large metallic Au component (82%) demonstrating the focus of the deposition products between the liquid phases. $[\text{AuCl}_4]^-$ (2%) and $[\text{AuCl}_2]^-$ (16%) are also shown to be present at the interface in the best fit.

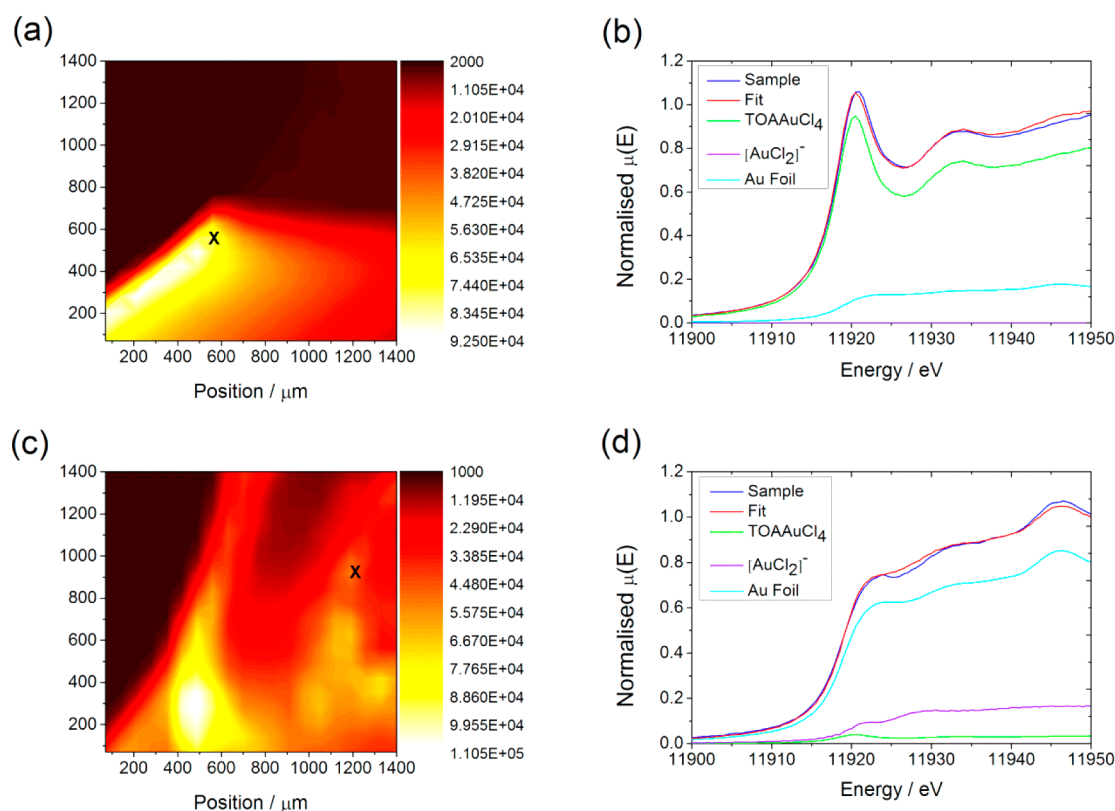


Figure 3. μ XRF maps of the L_3 edge at the liquid/liquid interface following the application of potential used to target XANES scans (a) in the organic bulk phase and (c) at the liquid/liquid interface. The positions of the XANES scans are marked by crosses. The XANES scans from the organic bulk (b) and the liquid/liquid interface (d) include a LCF and the weighted components.

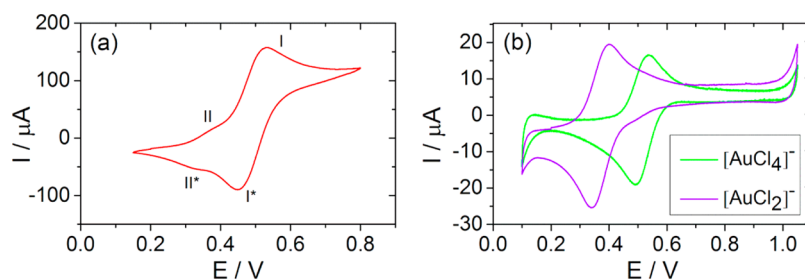


Figure 4. (a) CV of the droplet cell system showing the $[\text{AuCl}_4]^-$ and $[\text{AuCl}_2]^-$ ion transfer peaks. (b) CVs showing the ion transfer for $[\text{AuCl}_4]^-$ and $[\text{AuCl}_2]^-$ in the absence of reducing reagent. 5 mV s^{-1} scan rate. The lower currents observed in (b) are due to the lower concentrations used to measure the standards. Cell composition is defined in Table 1.

$[\text{AuCl}_2]^-$ was present as a small contribution (7–16%) in each of the interfacial samples analyzed. Inclusion of $[\text{AuCl}_2]^-$ improved the fit, as expressed by an R factor decrease from 0.0011 to 0.0010. The mismatch in the fit (R -factor) for the LCF with and without the inclusion of $[\text{AuCl}_2]^-$ is included in the Supporting Information (Table S1).

There is some variation between samples due to the heterogeneous nature of the system, arising from the spatial and temporal dependence of the Au speciation; however, as the LCF for each of the interfacial samples was improved by the inclusion of $[\text{AuCl}_2]^-$, the differences between fits are considered small enough to enable meaningful conclusions to be drawn. If the $[\text{AuCl}_2]^-$ fitted to the interfacial spectra was merely an artifact of the fit, rather than a physical feature, its presence would improve the bulk phase spectral fits, as well as those at the interface. However, the bulk phase LCF indicated that $[\text{AuCl}_2]^-$ was not a component of the data in the organic

phase—all LCFs of the bulk organic phase XANES showed a mixture of Au(III) and Au(0) without the presence of Au(I). XANES fits of the organic bulk phase and the liquid/liquid interface from the same μ XRF map are included in the Supporting Information (Figure S1). Au(I) has been detected in similar proportions against Au(III) and Au(0) by XANES during the X-ray-induced reduction of $[\text{AuCl}_4]^-$ in an aqueous solution.⁴⁵

In the liquid/liquid system it is not possible to generate EXAFS data with reliable signal-to-noise ratio when using the microfocused spot size. This is due to inhomogeneity in the sample due to clustering and aggregation of the nanoparticles. If this occurs on a length scale similar to the beam size (micron scale) then the nonlinear absorption, alongside the inhomogeneity in the beam itself, results in very noisy spectral responses which do not provide any reliable information.

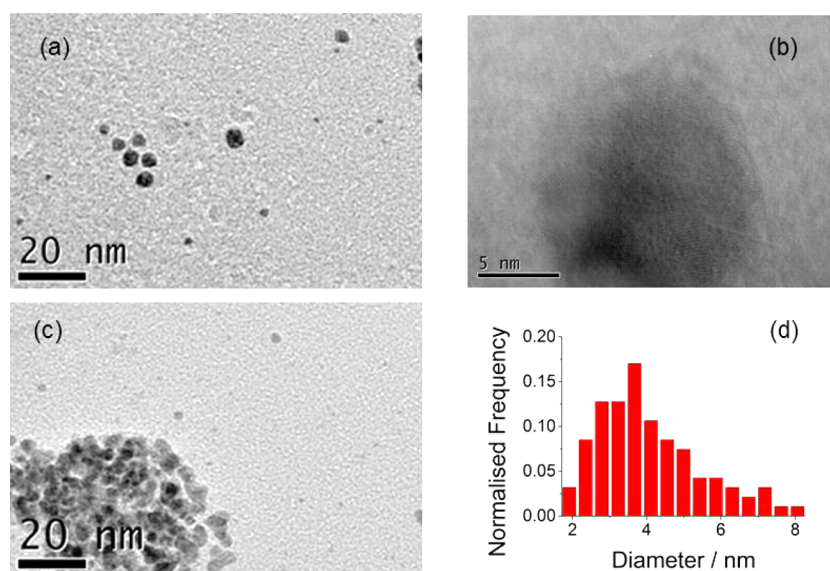


Figure 5. TEM images of the particles formed by potential-dependent deposition at the liquid/liquid interface: (a) isolated individual particles formed during the deposition, (b) higher magnification of an individual nanoparticle, (c) aggregated cluster of small particles, and (d) particle size distribution for isolated particles.

2.3. Cyclic Voltammetry. In the beamline experiment the potential was fixed in order to manipulate the position of the Au species enabling detection. For comparison, the system was also examined directly using cyclic voltammetry (CV). For the CV a standard liquid/liquid four-electrode cell (see Experimental Section) was used to reduce the volume of electrolyte solution required. A slightly acidic aqueous electrolyte (0.09 M LiCl + 10 mM HCl) was used in order to avoid the hydrolysis of the aqueous phase forming $[\text{AuCl}_3(\text{OH})]^-$.^{27,46} The CV (Figure 4a) clearly shows the presence of a large ion transfer peak corresponding to the transfer of $[\text{AuCl}_4]^-$ (peak I). The midpoint potential was found to be 0.49 V vs Ag/AgCl, and in the absence of TPTA it was 0.51 V. A second smaller peak is also visible (peak II) which is assigned to the ion transfer of $[\text{AuCl}_2]^-$ following the reduction of $[\text{AuCl}_4]^-$ by TPTA, the midpoint potential of this second peak cannot be obtained due to overlap with the transfer of Au(III). The electron transfer process was not detected in the region of the CV. The ion transfer potentials appear to agree with those for $[\text{AuCl}_4]^-$ and $[\text{AuCl}_2]^-$ in the absence of reducing reagent (Figure 4b). The intensity of the $[\text{AuCl}_2]^-$ ion transfer is much smaller than the $[\text{AuCl}_4]^-$ ion transfer which is in agreement with the 7–16% Au(I) concentration indicated by XANES analysis. There is a slight widening of the CV in the TOAAuCl₂ system at ~0.5 V due to the disproportionation of Au(I) in aqueous solution reforming a small quantity of Au(III).

2.4. Ex Situ Particle Analysis by TEM. The nanoparticles formed through the deposition protocol were extracted and examined using TEM (Figure 5). The images show that the particles formed are spherical (Figure 5a and 5b), with a tendency to form larger aggregates (Figure 5c). This aggregation of the particles occurs because the particles interact weakly with TOA⁺, acting as a stabilizing ligand.⁴⁷ The particle stability generated by the reduction in interfacial energy is better achieved by the aggregation of small nanoparticles than the growth of larger crystal structures. Particle growth may be halted at the most efficient point for reduction of the aqueous/organic interaction or possibly by the formation of “magic number” clusters which have a closed shell electronic

configuration aiding stability.^{43,48} The particle size distribution (Figure 5d) indicates an average particle diameter 3.9 ± 1.5 nm. Similar results have been achieved with other metal deposition studies at the liquid/liquid interface,⁴⁹ as reviewed by Rao and Kalyanikutty.⁵⁰ The TEM agrees well with the XAFS data showing a multiscattering peak at 11 946 eV which is indicative of particles >1 nm.^{41,51}

CONCLUSIONS

Gold deposition at the liquid/liquid interface has been examined by in situ μXRF and μXANES analysis. These data point to the isolation of the majority of the deposited gold at the liquid/liquid interface with some nanoparticles desorbing into the bulk phase. By probing the interface and the bulk phase, linear combination fitting of μXANES spectra reveals the formation of Au(I) as an intermediate species in the reduction of $[\text{AuCl}_4]^-$, by the organic electron donor TPTA, at the liquid/liquid interface. The observation of the presence of Au(I) is corroborated by cyclic voltammetry. This indicates that the reaction proceeds as shown in eq 3. The Au(0) detected spectroscopically, as determined by the large Au–Au multiscattering peak, corresponded to the formation of aggregate structures composed of spherical nanoparticles, as shown by TEM, which are predominantly present at the liquid/liquid interface.

EXPERIMENTAL METHODS

Chemicals. Bis(triphenylphosphoranylidene)ammonium chloride (BTPPACl, $\geq 98\%$), hydrogen tetrachloroaurate(III) hydrate (HAuCl_4 , 99.999%), lithium chloride ($\geq 99.99\%$), tri-*p*-tolylamine (TPTA, 97%), and 1,2-dichlorobenzene (1,2-DCB, $\geq 99\%$) were purchased from Sigma-Aldrich (Dorset, UK). Sodium tetrakis(trifluorophenyl)borate (NaTFPB , $\geq 97\%$) was supplied by Alfa Aesar (Lancashire, UK), hydrochloric acid (37%) by Fisher Scientific (Leicestershire, UK), and tetrabutylammonium dichloroaurate (TBAuCl_2) by Tokyo Chemical Industries Co. (Japan). The chemicals were used without further purification. The organic electrolyte BTPPATFPB was synthesized by metathesis of BTPPACl

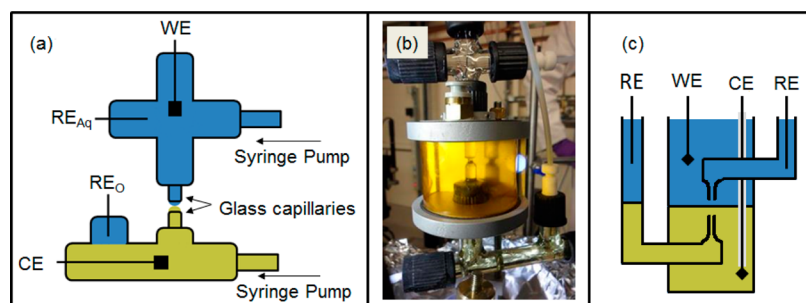


Figure 6. (a) Schematic of the windowless droplet cell; the aqueous phase is denoted as blue and the organic phase as yellow in the diagram. (b) Photograph of the windowless droplet cell in situ at the Diamond Light Source facility. (c) Schematic of the standard liquid/liquid cell used to conduct cyclic voltammetry.

Table 1. Liquid/Liquid Cell Composition

reference electrodes		aqueous phase		organic phase		organic reference		reference electrodes	
Ag(s)	AgCl(s)	0.1 M LiCl or 0.09 M LiCl + 10 mM HCl(aq)	4 mM TPTA, 4 mM TOAAuCl ₄	15 mM BTTPATFPB	10 mM LiCl, 1 mM BTTPACl(aq)	AgCl(s)	Ag(s)		

and NaTFPB as described previously.^{52,53} Tetraoctylammonium tetrachloroaurate (TOAAuCl₄) was synthesized by mixing TOACl and HAuCl₄ in ethanol then recrystallizing as detailed in ref 25. TOAAuCl₂ was produced by dissolving equimolar quantities of TBAAuCl₂ and TOACl in DCB and shaking with pure water, and the organic phase containing TOAAuCl₂ was then extracted. Ultrapure filtered water (Milli-Q, 18.2 MΩ cm resistivity) was used in the preparation of all aqueous solutions.

Electrochemistry. The reaction was conducted in a windowless liquid/liquid cell by making a contact between aqueous and organic phase droplets (Figure 6a and 6b).³⁸

A four-electrode cell setup was used with platinum flag counter electrodes and silver/silver chloride reference electrodes, which were made in house. The cell composition is indicated in Table 1.

To form the liquid/liquid interface in the droplet cell, the organic and aqueous phase droplets were brought into contact by pumping solution from the syringe in each phase as described previously.³⁸ The capillaries depicted in Figure 6(a) have an internal diameter of 4 mm. Following formation of the liquid/liquid interface a chronoamperometric pulse sequence initiated the deposition process. A conditioning potential of 0.1 V was applied (10 s), then 0.45 V was applied (15 s) in order to drive Au(III) ion transfer into the aqueous phase.³⁵ Finally the cell potential was fixed at 0.30 V (>200 s) to halt Au transfer while holding the Au(III) in the aqueous phase close to the interface, by stopping diffusion into the bulk phase, in order to enhance heterogeneous electron transfer between Au(III)(aq) and TPTA(org).

Cyclic voltammetry was conducted using the standard liquid/liquid electrochemical cell (Figure 6c), in this instance the acidified aqueous electrolyte was used. The scan rate was 5 mV s⁻¹, and *i*R compensation was applied during CV measurements.

Microfocus X-ray Fluorescence (μXRF) and X-ray Absorption Fine Structure (μXAFS). Experiments were conducted on the I18 microfocus beamline at the Diamond Light Source (Harwell Science and Innovation Campus, UK).⁵⁴ XRF maps were taken of the liquid/liquid interface, scanning each position for 1 s. The maps were always taken to the left of the droplet center in order to show the edge of the droplet. The response at this position is presumed to be identical to what

would be seen in the right-hand half of the droplet. Along with the variation in fluorescence intensity between the phases, the shape of the droplet helps to indicate the position of the interface. From the XRF map, the X-ray beam could be targeted for XANES analysis. The beam size was approximately 45 × 50 μm. The pixel size on the XRF maps was defined by the movement of the stage and was 70 × 70 μm. Data were collected on the Au L₃ edge using an Ortec multielement solid-state Ge detector and a Si(111) double-crystal monochromator. 2D maps of the liquid/liquid interface were collected by XRF, and then coordinates were chosen for XANES measurement. The XRF data were collected using an incident photon energy of 12 600 eV corresponding to absorption above the Au L₃ edge. The XANES data were treated and analyzed using the Athena program.⁵⁵ The standards for Au(III) (TOAAuCl₄ 5 mM in 1,2-DCB) and Au(0) (Au Foil) were collected at the beamtime. The Au(I) spectrum ([AuCl₂]⁻) was extracted from a number of TBAAuCl₂ spectra as described previously.²⁵

Transmission Electron Microscopy (TEM). Samples were collected on copper mesh holey carbon grids purchased from Agar Scientific (Agar Scientific Ltd. Essex, UK). Images were produced on a Philips CM200 TEM. Particle size distribution was determined using ImageJ software to analyze 94 nanoparticles. When calculating the particle size distribution only stand-alone particles were measured, and the aggregate clusters were not accounted for.

■ ASSOCIATED CONTENT

📄 Supporting Information

The Supporting Information contains a table showing the error in the XANES LFC in the presence and absence of Au(I), an example of XANES spectra taken from different positions on a single XRF map, and cyclic voltammetry showing scan rate dependence. The Supporting Information is available free of charge on the ACS Publications website at DOI: 10.1021/acs.jpcc.5b05127.

■ AUTHOR INFORMATION

Corresponding Authors

*E-mail: robert.dryfe@manchester.ac.uk.

*E-mail: s.l.m.schroeder@leeds.ac.uk.

Notes

The authors declare no competing financial interest.

ACKNOWLEDGMENTS

The authors would like to thank Diamond for the provision of beamtime – SP8861. A.U. would like to acknowledge support by the Kyoto University Foundation. RAWD and SLMS thank the EPSRC for financial support via an EPSRC-NSF “Materials World Network” grant (EP/H047786/1). SYC gratefully acknowledges the award of a President’s PhD Scholarship by the University of Manchester. The authors would also like to thank Rebecca Mackenzie, Frank Booth, and Tina Holley for their constructive suggestions on the text of the manuscript.

REFERENCES

- (1) Turkevich, J.; Stevenson, P. C.; Hillier, J. A Study of the Nucleation and Growth Processes in the Synthesis of Colloidal Gold. *Discuss. Faraday Soc.* **1951**, *11*, 55–75.
- (2) Frens, G. Controlled Nucleation for Regulation of Particle-Size in Monodisperse Gold Suspensions. *Nature, Phys. Sci.* **1973**, *241*, 20–22.
- (3) Brust, M.; Walker, M.; Bethell, D.; Schiffrin, D. J.; Whyman, R. Synthesis of Thiol-Derivatized Gold Nanoparticles in a 2-Phase Liquid-Liquid System. *J. Chem. Soc., Chem. Commun.* **1994**, *7*, 801–802.
- (4) Brust, M.; Fink, J.; Bethell, D.; Schiffrin, D. J.; Kiely, C. Synthesis and Reactions of Functionalised Gold Nanoparticles. *J. Chem. Soc., Chem. Commun.* **1995**, *16*, 1655–1656.
- (5) Lee, P. C.; Meisel, D. Adsorption and Surface-Enhanced Raman of Dyes on Silver and Gold Sols. *J. Phys. Chem.* **1982**, *86*, 3391–3395.
- (6) Zhao, P. X.; Li, N.; Astruc, D. State of the Art in Gold Nanoparticle Synthesis. *Coord. Chem. Rev.* **2013**, *257*, 638–665.
- (7) Zheng, H. M.; Smith, R. K.; Jun, Y. W.; Kisielowski, C.; Dahmen, U.; Alivisatos, A. P. Observation of Single Colloidal Platinum Nanocrystal Growth Trajectories. *Science* **2009**, *324*, 1309–1312.
- (8) Goulet, P. J. G.; Lennox, R. B. New Insights into Brust-Schiffrin Metal Nanoparticle Synthesis. *J. Am. Chem. Soc.* **2010**, *132*, 9582–9584.
- (9) Perala, S. R. K.; Kumar, S. On the Mechanism of Metal Nanoparticle Synthesis in the Brust-Schiffrin Method. *Langmuir* **2013**, *29*, 9863–9873.
- (10) Yu, C. H.; Zhu, L. L.; Zhang, R. C.; Wang, X. L.; Guo, C. C.; Sun, P. C.; Xue, G. Investigation on the Mechanism of the Synthesis of Gold(I) Thiolate Complexes by NMR. *J. Phys. Chem. C* **2014**, *118*, 10434–10440.
- (11) Moller, F. A.; Kintrop, J.; Lachenwitzer, A.; Magnussen, O. M.; Behm, R. J. In situ STM Study of the Electrodeposition and Anodic Dissolution of Ultrathin Epitaxial Ni Films on Au(111). *Phys. Rev. B: Condens. Matter Mater. Phys.* **1997**, *56*, 12506–12518.
- (12) Brankovic, S. R.; Wang, J. X.; Adzic, R. R. Metal Monolayer Deposition by Replacement of Metal Adlayers on Electrode Surfaces. *Surf. Sci.* **2001**, *474*, 173–179.
- (13) Liu, H.; Favier, F.; Ng, K.; Zach, M. P.; Penner, R. M. Size-Selective Electrodeposition of Meso-Scale Metal Particles: A General Method. *Electrochim. Acta* **2001**, *47*, 671–677.
- (14) Walter, E. C.; Zach, M. P.; Favier, F.; Murray, B. J.; Inazu, K.; Hemminger, J. C.; Penner, R. M. Metal Nanowire Arrays by Electrodeposition. *ChemPhysChem* **2003**, *4*, 131–138.
- (15) Cheng, Y. F.; Schiffrin, D. J. Electrodeposition of Metallic Gold Clusters at the Water/1,2-dichloroethane Interface. *J. Chem. Soc., Faraday Trans.* **1996**, *92*, 3865–3871.
- (16) Trojanek, A.; Langmaier, J.; Samec, Z. Random Nucleation and Growth of Pt Nanoparticles at the Polarised Interface Between Two Immiscible Electrolyte Solutions. *J. Electroanal. Chem.* **2007**, *599*, 160–166.
- (17) Johans, C.; Liljeroth, P.; Kontturi, K. S. Electrodeposition at Polarizable Liquid Vertical Bar Liquid Interfaces: The Role of

Interfacial Tension on Nucleation Kinetics. *Phys. Chem. Chem. Phys.* **2002**, *4*, 1067–1071.

(18) Platt, M.; Dryfe, R. A. W.; Roberts, E. P. L. Controlled Deposition of Nanoparticles at the Liquid-Liquid Interface. *Chem. Commun.* **2002**, *20*, 2324–2325.

(19) Guainazzi, M.; Silvestri, G.; Serravalle, G. Electrochemical Metallization at Liquid-Liquid Interfaces of Non-Miscible Electrolytic Solutions. *J. Chem. Soc., Chem. Commun.* **1975**, *6*, 200–201.

(20) Guo, J. D.; Tokimoto, T.; Othman, R.; Unwin, P. R. Formation of Mesoscopic Silver Particles at Micro- and Nano-Liquid/Liquid Interfaces. *Electrochem. Commun.* **2003**, *5*, 1005–1010.

(21) Gründer, Y.; Ramasse, Q. M.; Dryfe, R. A. W. A Facile Electrochemical Route to the Preparation of Uniform and Monoatomic Copper Shells for Gold Nanoparticles. *Phys. Chem. Chem. Phys.* **2015**, *17*, 5565–5568.

(22) Schmidt, U.; Donten, M.; Osteryoung, J. G. Gold Electrocrystallization on Carbon and Highly Oriented Pyrolytic Graphite from Concentrated Solutions of LiCl. *J. Electrochem. Soc.* **1997**, *144*, 2013–2021.

(23) Gammons, C. H.; Yu, Y. M.; Williams-Jones, A. E. The Disproportionation of Gold(I) Chloride Complexes at 25 to 200 Degrees C. *Geochim. Cosmochim. Acta* **1997**, *61*, 1971–1983.

(24) Uehara, A.; Hashimoto, T.; Dryfe, R. A. W. Au Electrodeposition at the Liquid-Liquid Interface: Mechanistic Aspects. *Electrochim. Acta* **2014**, *118*, 26–32.

(25) Chang, S. Y.; Uehara, A.; Booth, S. G.; Ignatyev, K.; Mosselmans, J. F. W.; Dryfe, R. A. W.; Schroeder, S. L. M. Structure and Bonding in Au(I) Chloride Species: A Critical Examination of X-ray Absorption Spectroscopy (XAS) Data. *RSC Adv.* **2015**, *5*, 6912–6918.

(26) Henglein, A. Radiolytic Preparation of Ultrafine Colloidal Gold Particles in Aqueous Solution: Optical Spectrum, Controlled Growth, and Some Chemical Reactions. *Langmuir* **1999**, *15*, 6738–6744.

(27) Usher, A.; McPhail, D. C.; Brugger, J. A Spectrophotometric Study of Aqueous Au(III) Halide-Hydroxide Complexes at 25–80 Degrees C. *Geochim. Cosmochim. Acta* **2009**, *73*, 3359–3380.

(28) Holt, K. B.; Sabin, G.; Compton, R. G.; Foord, J. S.; Marken, F. Reduction of Tetrachloroaurate (III) at Boron-Doped Diamond Electrodes: Gold Deposition Versus Gold Colloid Formation. *Electroanalysis* **2002**, *14*, 797–803.

(29) Boxley, C. J.; White, H. S.; Lister, T. E.; Pinhero, P. J. Electrochemical Deposition and Reoxidation of Au at Highly Oriented Pyrolytic Graphite. Stabilization of Au Nanoparticles on the Upper Plane of Step Edges. *J. Phys. Chem. B* **2003**, *107*, 451–458.

(30) Martin, H.; Carro, P.; Creus, A. H.; Gonzalez, S.; Salvezza, R. C.; Arvia, A. J. Growth Mode Transition Involving a Potential-Dependent Isotropic to Anisotropic Surface Atom Diffusion Change. Gold Electrodeposition on HOPG Followed by STM. *Langmuir* **1997**, *13*, 100–110.

(31) Goolsby, A. D.; Sawyer, D. T. Electrochemistry of Gold(I) and its Complexes in Acetonitrile. *Anal. Chem.* **1968**, *40*, 1978–1983.

(32) Koelle, U.; Laguna, A. Electrochemistry of Au-Complexes. *Inorg. Chim. Acta* **1999**, *290*, 44–50.

(33) Aldous, L.; Silvester, D. S.; Villagran, C.; Pitner, W. R.; Compton, R. G.; Lagunas, M. C.; Hardacre, C. Electrochemical Studies of Gold and Chloride in Ionic Liquids. *New J. Chem.* **2006**, *30*, 1576–1583.

(34) Monzon, L. M. A.; Byrne, F.; Coey, J. M. D. Gold Electrodeposition in Organic Media. *J. Electroanal. Chem.* **2011**, *657*, 54–60.

(35) Gründer, Y.; Ho, H. L. T.; Mosselmans, J. F. W.; Schroeder, S. L. M.; Dryfe, R. A. W. Inhibited and Enhanced Nucleation of Gold Nanoparticles at the Water Vertical Bar 1,2-dichloroethane Interface. *Phys. Chem. Chem. Phys.* **2011**, *13*, 15681–15689.

(36) Dryfe, R. A. W.; Uehara, A.; Booth, S. G. Metal Deposition at the Liquid-Liquid Interface. *Chem. Rec.* **2014**, *14*, 1013–1023.

(37) Grunwaldt, J. D.; Wagner, J. B.; Dunin-Borkowski, R. E. Imaging Catalysts at Work: A Hierarchical Approach from the Macro- to the Meso- and Nano-scale. *ChemCatChem* **2013**, *5*, 62–80.

(38) Gründer, Y.; Mosselmans, J. F. W.; Schroeder, S. L. M.; Dryfe, R. A. W. In Situ Spectroelectrochemistry at Free-Standing Liquid-Liquid Interfaces: UV-vis Spectroscopy, Microfocus X-ray Absorption Spectroscopy, and Fluorescence Imaging. *J. Phys. Chem. C* **2013**, *117*, 5765–5773.

(39) Yurchenko, O.; Freytag, D.; Borg, L. Z.; Zentel, R.; Heinze, J.; Ludwigs, S. Electrochemically Induced Reversible and Irreversible Coupling of Triarylaminines. *J. Phys. Chem. B* **2012**, *116*, 30–39.

(40) Ohyama, J.; Teramura, K.; Higuchi, Y.; Shishido, T.; Hitomi, Y.; Kato, K.; Tanida, H.; Uruga, T.; Tanaka, T. In Situ Observation of Nucleation and Growth Process of Gold Nanoparticles by Quick XAFS Spectroscopy. *ChemPhysChem* **2011**, *12*, 127–131.

(41) Pucci, A.; Tirelli, N.; Willneff, E. A.; Schroeder, S. L. M.; Galembeck, F.; Ruggeri, G. Evidence and Use of Metal-Chromophore Interactions: Luminescence Dichroism of Terthiophene-Coated Gold Nanoparticles in Polyethylene Oriented Films. *J. Mater. Chem.* **2004**, *14*, 3495–3502.

(42) Binks, B. P.; Lumsdon, S. O. Influence of Particle Wettability on the Type and Stability of Surfactant-Free Emulsions. *Langmuir* **2000**, *16*, 8622–8631.

(43) Lin, Y.; Skaff, H.; Emrick, T.; Dinsmore, A. D.; Russell, T. P. Nanoparticle Assembly and Transport at Liquid-Liquid Interfaces. *Science* **2003**, *299*, 226–229.

(44) Dryfe, R. A. W. Modifying the Liquid/Liquid Interface: Pores, Particles and Deposition. *Phys. Chem. Chem. Phys.* **2006**, *8*, 1869–1883.

(45) Ma, Q.; Divan, R.; Mancini, D. C.; Keane, D. T. Elucidating Chemical and Morphological Changes in Tetrachloroauric Solutions Induced by X-ray Photochemical Reaction. *J. Phys. Chem. A* **2008**, *112*, 4568–4572.

(46) Durovic, M. D.; Puchta, R.; Bugarcic, Z. D.; van Eldik, R. Studies on the Reactions of AuCl_4^- with Different Nucleophiles in Aqueous Solution. *Dalton Trans.* **2014**, *43*, 8620–8632.

(47) Reetz, M. T.; Helbig, W. Size-Selective Synthesis of Nanostructured Transition-Metal Clusters. *J. Am. Chem. Soc.* **1994**, *116*, 7401–7402.

(48) Howie, A. Blazing the Trail from Metals to Nuclei. *Faraday Discuss.* **1991**, *92*, 1–11.

(49) Platt, M.; Dryfe, R. A. W. Structural and Electrochemical Characterisation of Pt and Pd Nanoparticles Electrodeposited at the Liquid/Liquid Interface: Part 2. *Phys. Chem. Chem. Phys.* **2005**, *7*, 1807–1814.

(50) Rao, C. N. R.; Kalyanikutty, K. P. The Liquid-Liquid Interface as a Medium to Generate Nanocrystalline Films of Inorganic Materials. *Acc. Chem. Res.* **2008**, *41*, 489–499.

(51) Lengke, M. F.; Ravel, B.; Fleet, M. E.; Wanger, G.; Gordon, R. A.; Southam, G. Mechanisms of Gold Bioaccumulation by Filamentous Cyanobacteria from Gold(III) - Chloride Complex. *Environ. Sci. Technol.* **2006**, *40*, 6304–6309.

(52) Fermin, D. J.; Duong, H. D.; Ding, Z. F.; Brevet, P. F.; Girault, H. H. Photoinduced Electron Transfer at Liquid/Liquid Interfaces - Part II. A Study of the Electron Transfer and Recombination Dynamics by Intensity Modulated Photocurrent Spectroscopy (IMPS). *Phys. Chem. Chem. Phys.* **1999**, *1*, 1461–1467.

(53) Vanysek, P.; Novak, V. Liquid/Liquid Electrochemistry in Electroanalysis: Fundamentals Revisited. *ECS Trans.* **2009**, *19*, 55–63.

(54) Mosselmans, J. F. W.; Quinn, P. D.; Dent, A. J.; Cavill, S. A.; Moreno, S. D.; Peach, A.; Leicester, P. J.; Keylock, S. J.; Gregory, S. R.; Atkinson, K. D.; et al. I18-the Microfocus Spectroscopy Beamline at the Diamond Light Source. *J. Synchrotron Radiat.* **2009**, *16*, 818–824.

(55) Ravel, B.; Newville, M. Athena, Artemis, Hephaestus: Data Analysis for X-ray Absorption Spectroscopy using IFEFFIT. *J. Synchrotron Radiat.* **2005**, *12*, 537–541.